

Evolution of finite-amplitude localized vortices in planar homogeneous shear flows

Michael Karp*

Faculty of Aerospace Engineering, Technion–Israel Institute of Technology, Haifa 32000, Israel

Ilya G. Shukhman

Institute of Solar-Terrestrial Physics, Russian Academy of Sciences, Siberian Department, Irkutsk 664033, P.O. Box 291, Russia

Jacob Cohen

Faculty of Aerospace Engineering, Technion–Israel Institute of Technology, Haifa 32000, Israel

(Received 6 September 2016; published 13 February 2017)

An analytical-based method is utilized to follow the evolution of localized initially Gaussian disturbances in flows with homogeneous shear, in which the base velocity components are at most linear functions of the coordinates, including hyperbolic, elliptic, and simple shear. Coherent structures, including counterrotating vortex pairs (CVPs) and hairpin vortices, are formed for the cases where the streamlines of the base flow are open (hyperbolic and simple shear). For hyperbolic base flows, the dominance of shear over rotation leads to elongation of the localized disturbance along the outlet asymptote and formation of CVPs. For simple shear CVPs are formed from linear and nonlinear disturbances, whereas hairpins are observed only for highly nonlinear disturbances. For elliptic base flows CVPs, hairpins and vortex loops form initially, however they do not last and break into various vortical structures that spread in the spanwise direction. The effect of the disturbance's initial amplitude and orientation is examined and the optimal orientation achieving maximal growth is identified.

DOI: [10.1103/PhysRevFluids.2.024701](https://doi.org/10.1103/PhysRevFluids.2.024701)

I. INTRODUCTION

Coherent vortical structures observed in turbulent boundary layers have been reported as early as 1967 [1]. In this pioneering work two kinds of coherent structures were identified: (i) counterrotating vortex pairs (CVPs), which lead to the creation of streaks (regions of high and low velocity), and (ii) hairpin (or horseshoe) vortices, which consist of a pair of streamwise vortices connected by a short spanwise head segment. The remarkable feature of these structures is that their properties seem to be universal through a range of flows and Reynolds numbers, e.g., the spanwise separation between the vortices of the CVP was found to be about 100 wall units [1,2] and the hairpin vortex was found to be inclined approximately 45° relative to the base flow [3], as first suggested by Theodorsen [4]. Since then, a growing list of researchers have reported the existence of these coherent structures in a variety of wall-bounded turbulent and transitional shear flows. A good summary of the experimental and numerical findings regarding the coherent structures can be found in the review by Robinson [5] as well as the introduction of Schoppa and Hussain [6].

Counterrotating vortex pairs have been found to generate transient growth [7] through the creation of streaks. During the transient growth the flow may become susceptible to secondary instabilities (see, e.g., [8]). Hairpins have been identified in transitional scenarios where the flow undergoes secondary varicose instabilities (see, e.g., [9]). The secondary instabilities led to incorporation of CVPs as part of the self-sustained process (instability based) proposed by Waleffe [10]. A different

*Corresponding author: mkarp@technion.ac.il

self-sustained cycle proposed by Schoppa and Hussain [6] consists of interactions between parent and offspring hairpins. More recently, hairpins have been identified as nonlinear optimal structures on the route to turbulence [11]. One of the approaches towards understanding the physics of these structures has been to study the evolution of artificially generated structures in laminar flows. Hairpins were generated using a hemispheric bump (e.g., boundary layer [12]) and injection (e.g., boundary layer [13] and Taylor-Couette flow [14]). It has been found that, although the flow is laminar and does not contain the turbulent Reynolds stress, similarities between the evolution of the vortical shapes and inclination angles of 45° have been observed. Studies of streamwise vortices have found that the spanwise and streamwise dimensions are comparable between transitional and turbulent boundary layer flows [15,16].

The appearance of these structures under various flow conditions suggests that these structures may play a key role in various transition scenarios and self-sustained turbulence. Moreover, the similarities between the structures may imply that they are generated by a basic mechanism that relies on the common elements of the flows: the shear of the base flow and the presence of a localized vortical disturbance. In recent years, having in mind this mechanism, a simple model following the evolution of the aforementioned coherent structures has been developed [17–20]. The model follows the evolution of localized disturbances (in space) embedded in homogeneous shear flows. The main assumption in these studies is that the disturbance is localized and therefore “sees” only the homogeneous shear surrounding it, i.e., the velocity components of the surrounding base flow are at most linear functions of the coordinates. The linear and nonlinear evolution of localized vortical disturbances embedded in simple shear (unbounded Couette) flow were investigated in Ref. [17]. It was found that for sufficiently low initial amplitudes CVPs are generated, whereas for sufficiently high initial amplitudes hairpins are formed. Similarities between the characteristics of coherent vortices, such as the inclination angles and convective velocities, have been reported. The model has also been employed for plane stagnation (irrotational) flow to study linear and nonlinear effects in the formation of CVPs [18].

The evolution (linear and nonlinear) of localized vortical disturbances in the above studies [17,18] has been calculated using the commercial direct numerical simulation (DNS) software FLUENT. Nevertheless, assuming linear (small-amplitude) disturbances, the evolution of localized disturbances can be solved analytically. The linear evolution of localized disturbances in plane shear flows has been solved analytically for plane stagnation (irrotational) flow [21], simple shear [22], circular shear flow [23], hyperbolic flow [19] (see definition in Sec. III A), and elliptic flow [20]. For simple shear the linear analysis has revealed that the vortical disturbances evolve into CVPs that gradually align with the x axis. Since the flow is linearly stable, the growth is transient for the viscous case and initially behaves according to a power law. It has been established that for optimal disturbance growth the initial angles of the vortex plane are between 115° and 135° relative to the positive x axis. The viscosity affects the maximal growth and the instant of time when this maximal growth is reached, however the qualitative evolution of the vortex is less affected by the viscosity. The analysis has also shown that hairpin vortices cannot be obtained in the linear case due to the symmetry properties of the equations. For hyperbolic flows, the linear analysis has revealed that the vortices evolve into CVPs, which extend along the principal axis of elongation (the outlet asymptote). The strength of the vortical disturbances grows exponentially. The most amplified vortices for this case are those having the vortex plane initially oriented around the angles 120° – 150° relative to the positive x axis. Linear analysis of disturbances embedded in elliptic flows has shown that for circular (pure-rotational) flow there is pure attenuation, whereas for all other types of elliptic flows exponential growth may be expected (both viscous and inviscid). However, the final exponential growth may be preceded by a long finite-time attenuation. Thus, for a finite observation time amplification may occur only for a certain range of elliptic flows and there exists an optimal elliptic flow for which the amplification is the most rapid. Analysis of the obtained structures has not revealed the aforementioned coherent structures, but rather two basic regions of vorticity localizations with two additional vorticity regions that appear and disappear periodically.

Recently, utilizing concepts from the analytical solution for linear disturbances, an analytical-based numerical method (ABNM) has been developed [24], capable of following the nonlinear

evolution of finite-amplitude localized disturbances embedded in any homogeneous shear flow. The solution is carried out using Lagrangian variables in Fourier space, which enables very efficient computations relative to other DNS software. The method has been implemented using MATLAB and compared successfully with previous results mentioned above [17,18]. Comparing the ABNM to other DNS software (e.g., FLUENT), the ABNM is limited by the requirement that the shear of the base flow is homogeneous. Nevertheless, other DNS software demands more calculation time and requires writing programs for the insertion and extraction of initial disturbance and further postprocessing, which are easily performed in the ABNM. The ABNM has also been utilized to follow the evolution of a train of hairpins in a minimal flow-element model [25], consisting of simple shear, CVPs, and a wavy vortex sheet.

The aim of the present paper is to explore the nonlinear evolution of localized disturbances in various homogeneous shear base flows (hyperbolic, simple shear, and elliptic), taking advantage of the ABNM. In particular, we aim to study the effects of base-flow shear and vorticity as well as the initial disturbance magnitude and orientation. The mathematical method is briefly summarized in Sec. II, followed by results in Sec. III, and a discussion and summary in Sec. IV. Appendix A summarizes the numerical parameters used for the calculations, whereas Appendix B presents the analytical expressions describing the linear evolution of the total enstrophy in hyperbolic flows.

II. MATHEMATICAL METHOD

A. Analytical-based numerical method

The ABNM is described thoroughly in Ref. [24], thus only essential features of the method are given here. Without loss of generality the base-flow velocity and vorticity are given by

$$\mathbf{V} = \left(-\frac{1}{2}(\Omega + \sigma)y, -\frac{1}{2}(\sigma - \Omega)x, 0\right), \quad \boldsymbol{\Omega} = (0, 0, \Omega), \quad (1)$$

where σ and Ω are constants representing the base-flow strain rate and vorticity, respectively. The equation describing the evolution of vorticity $\boldsymbol{\omega}$ associated with a three-dimensional finite-amplitude localized disturbance in incompressible viscous base flow is

$$\frac{\partial \boldsymbol{\omega}}{\partial t} + (\mathbf{V} \cdot \nabla) \boldsymbol{\omega} - (\boldsymbol{\omega} \cdot \nabla) \mathbf{V} - (\boldsymbol{\Omega} \cdot \nabla) \mathbf{v} = \nu \Delta \boldsymbol{\omega} + (\boldsymbol{\omega} \cdot \nabla) \mathbf{v} - (\mathbf{v} \cdot \nabla) \boldsymbol{\omega}, \quad (2)$$

where t is time, ν is the kinematic viscosity, and the disturbance vorticity $\boldsymbol{\omega}$ and velocity \mathbf{v} are related by $\boldsymbol{\omega} = \nabla \times \mathbf{v}$. The two rightmost terms on the right-hand side are the nonlinear terms. The equations are transformed to ordinary differential equations (in time) by performing a transformation from real space [$\mathbf{r} = (x, y, z)$] to Fourier space [$\mathbf{k} = (k_1, k_2, k_3)$] and using Lagrangian variables [$\mathbf{q} = (q_1, q_2, q_3)$]. The equations are integrated in time using Euler's method (first order) and the vorticity in real space is calculated by applying the inverse Fourier transform. The following parameters are defined for convenient comparison between various base flows:

$$\kappa = \frac{1}{2} \sqrt{\sigma^2 - \Omega^2} \quad (\text{for } \sigma^2 > \Omega^2), \quad \eta = \frac{1}{2} \sqrt{\Omega^2 - \sigma^2} \quad (\text{for } \Omega^2 > \sigma^2); \quad (3)$$

$$\lambda = \frac{\sigma - \Omega}{\sigma + \Omega}, \quad \Omega_* = \frac{|\sigma| + |\Omega|}{2}. \quad (4)$$

B. Initial disturbance

Following previous studies [17–20,22,23], the initial disturbance used in this study is the Gaussian disturbance given by the following expression:

$$\boldsymbol{\omega}(\mathbf{r}, t = 0) = \nabla F \times \boldsymbol{\mu}, \quad F = (\pi^{1/2} \delta)^{-3} \exp(-r^2/\delta^2), \quad (5)$$

where r is the spherical radial coordinate, δ is the representative length scale of the disturbance, and $\boldsymbol{\mu}$ is its initial fluid impulse. We focus on disturbances that are symmetric with respect to the spanwise coordinate, i.e., $\boldsymbol{\mu} = (\mu_1, \mu_2, 0)$. The initial orientation of the vortex ϕ is the angle between

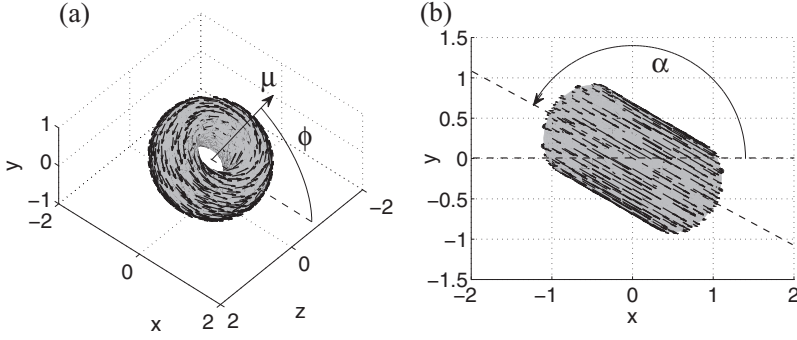


FIG. 1. Isosurface ($|\omega| = 0.7\omega_{\max}$) of the initial Gaussian disturbance with the vorticity vectors superimposed: (a) illustration of fluid impulse μ and its orientation ϕ and (b) illustration of vortex inclination angle α .

μ and the positive x axis, i.e., $\tan \phi = \mu_2/\mu_1$. The strength of the initial vortex is characterized by $\varepsilon = \omega_{\max}(t=0)/\Omega_*$, where for a Gaussian vortex $\omega_{\max}(t=0) = 0.154\mu/\delta^4$. The magnitude of ε determines whether the nonlinear terms are negligible (i.e., $\varepsilon \ll 1$). All length scales are normalized by δ and the time scale by $1/\Omega_*$. The vortex Reynolds number is given by $\text{Re} = \Omega_*\delta^2/\nu$. It should be noted that the corresponding Reynolds number based on a representative length scale of the base flow Δ and a representative velocity of the base flow $\Omega_*\Delta$ is $\text{Re}_\Delta = (\Delta/\delta)^2\text{Re}$, which is much larger than the vortex Reynolds number. The initial disturbance (plotted for arbitrary parameters) is presented in Fig. 1. An isosurface corresponding to $0.7\omega_{\max}$ is shown, with the vorticity vectors superimposed. The fluid impulse μ and initial orientation angle ϕ are illustrated in Fig. 1(a).

C. Integral properties

The strength of the vortex is measured by the volumetric integral of enstrophy (also referred to as the total enstrophy)

$$W(t) = \int_V |\omega|^2 dV. \quad (6)$$

For the Gaussian disturbance $W(0) = (2\pi^3)^{-1/2}\mu^2/\delta^5$. Additional integral properties proposed by Shukhman and Levinski [22] include the center of the vortical structure (CVS) and the vortex inclination angle α , which describes the angle between the vortex elongation axis and the x axis. The CVS is the first moment of the enstrophy, normalized by the vortex strength (this definition is analogous to center of gravity)

$$X_i(t) = \frac{\int_V |\omega|^2 x_i dV}{W(t)}. \quad (7)$$

The vortex inclination angle for spanwise symmetric disturbances is defined by

$$\alpha = \frac{1}{2} \arctan\left(\frac{2T_{12}}{T_{11} - T_{22}}\right) + \frac{1}{4}\pi(1+s) - \frac{1}{2}\pi, \quad s = \text{sgn}(T_{11} - T_{22}), \quad (8)$$

where T_{ij} is the tensor of enstrophy distribution defined as (see [22])

$$T_{ij} = \int_V |\omega|^2 (x_i - X_i)(x_j - X_j) dV. \quad (9)$$

Thus, α is the angle between the longest principal axis of T_{ij} and the x axis, as illustrated in Fig. 1(b) for the initial disturbance.

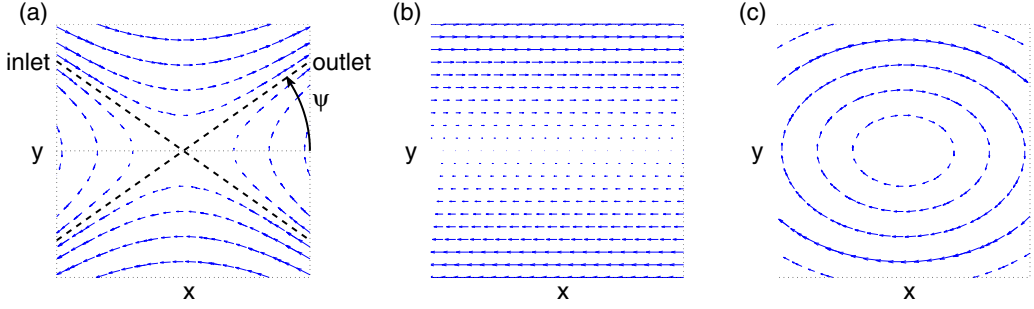


FIG. 2. Base-flow examples: (a) hyperbolic, $\lambda = 0.5$, with inlet and outlet asymptotes superimposed; (b) simple shear, $\lambda = 0$; and (c) elliptic, $\lambda = -0.5$.

III. RESULTS

A. Parameter definition

As mentioned in the Introduction, three types of homogeneous shear flows exist. (a) One is hyperbolic flow for $|\sigma| > |\Omega|$ ($\lambda > 0$), having hyperbolic streamlines and two asymptotes with angles $\psi = \pm \arctan(\lambda^{1/2})$, corresponding to the outlet (+) and the inlet (-) directions. The limiting case of this flow is the irrotational (plane stagnation) flow with $\Omega = 0$ ($\lambda = 1$). Hyperbolic flows are found in a mixing layer between two consecutive Kelvin-Helmholtz rollers (see Fig. 1 in Ref. [24]). Other applications of hyperbolic flows are described in detail in the introduction of [26], (b) simple shear for $\sigma = \Omega$ ($\lambda = 0$), which is the unbounded Couette flow, and (c) elliptic flow for $|\sigma| < |\Omega|$ ($\lambda < 0$), having elliptic streamlines, with the limiting case of pure rotational flow for $\sigma = 0$ ($\lambda = -1$). Elliptic flows may serve as approximations of flows around one-dimensional vortex cores. Additional examples are given in Refs. [27,28]. In the current study several base flows are examined by varying $\sigma < 0$ and $\Omega < 0$ to obtain $\lambda = (-1, -0.75, -0.5, \dots, 1)$, while maintaining a constant value of $\Omega_* = 40 \text{ s}^{-1}$. The three types of flow are presented in Fig. 2. The inlet and outlet asymptotes for hyperbolic flow [Fig. 2(a)] are superimposed on the figure, together with the angle ψ . The simple shear is plotted in Fig. 2(b) and the elliptic flow is in Fig. 2(c). The rotation frequency of a fluid particle over an elliptic streamline is $\eta = 2\pi/T_{\text{ell}}$, where η is defined in Eq. (3) and T_{ell} is the rotation period.

For each base flow various initial orientations and initial amplitudes of the disturbance are examined. The vortex initial orientation is varied as $\phi = (0^\circ, 10^\circ, 20^\circ, \dots, 180^\circ)$. The initial orientation is physically interesting since it has a major effect on the evolution of the vortex. Depending on the orientation, the vortex may decay initially or grow rapidly. One can also find the optimal initial orientation that causes maximal amplification for a given time. The initial amplitude of the vortex ε is varied between $\varepsilon = 0.015, 1, \text{ and } 7.5$, corresponding to linear, moderately nonlinear (MNL), and highly nonlinear (HNL) cases, respectively. The simulations are performed for $\delta = 10^{-3} \text{ m}$ and $\nu = 10^{-6} \text{ m}^2/\text{s}$, which together with $\Omega_* = 40 \text{ s}^{-1}$ maintain a vortex Reynolds number of $\text{Re} = 40$ for all the cases. Due to the large number of parameters, the effect of varying Re is left for a future study. The numerical parameters are summarized in Appendix A. Convergence has been verified by obtaining negligible differences in the evolution as a result of doubling the computational domain size for a fixed cell size and doubling the number of points in each direction for a fixed domain (i.e., fixed domain with half-cell size).

B. Parametric investigation

1. Hyperbolic flows

For all hyperbolic flows ($\lambda > 0$) similar features of the disturbance evolution are observed for various values of λ . Moreover, the overall evolution is very similar for linear and MNL disturbances;

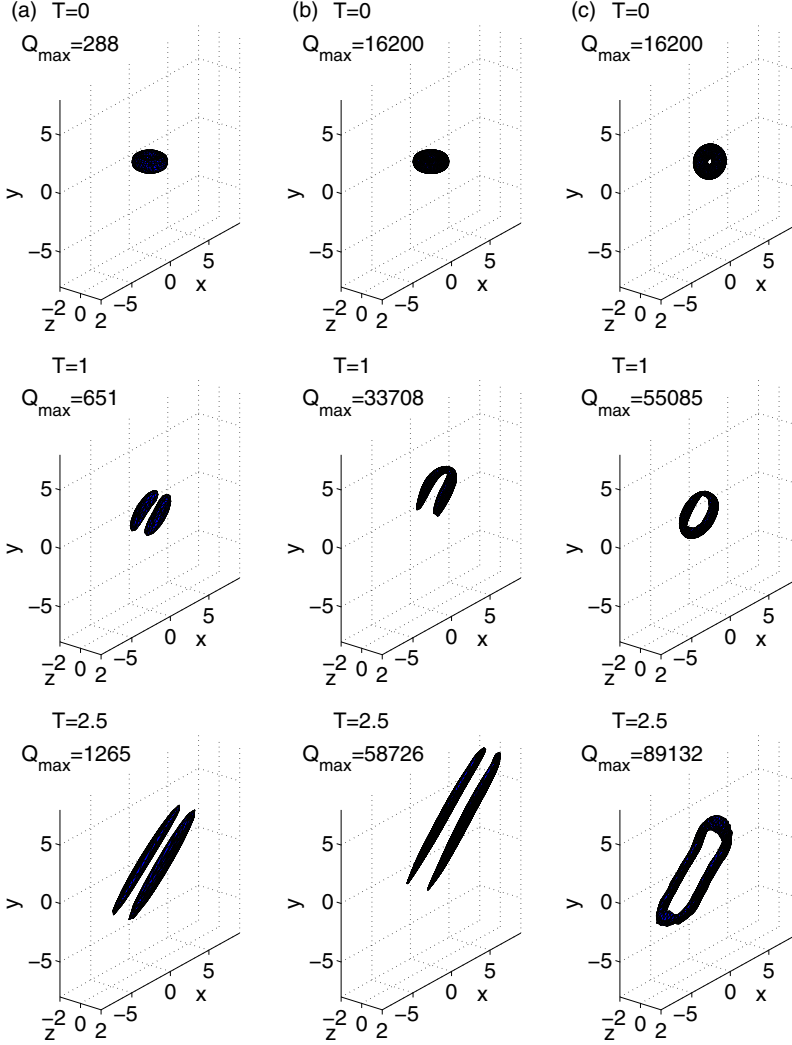


FIG. 3. Disturbance evolution for $\lambda = 0.5$, isosurfaces of $Q/Q_{\max} = 0.3$ for (a) $\varepsilon = 1$ (MNL) and $\phi = 90^\circ$, (b) $\varepsilon = 7.5$ (HNL) and $\phi = 90^\circ$, and (c) $\varepsilon = 7.5$ (HNL) and $\phi = 150^\circ$.

in both cases the disturbance evolves into CVPs that elongate along the outlet asymptote. An example is presented in Fig. 3(a) for $\lambda = 0.5$ and $\phi = 90^\circ$. The second invariant of the velocity gradient tensor $Q = (-\frac{1}{2}\partial u_i/\partial x_j)(\partial u_j/\partial x_i)$; (see [29]) is visualized to capture regions of swirling motion. Initially, the MNL disturbance evolves into CVPs ($T = 1$) and then the vortices are stretched by the base flow ($T = 2.5$).

The HNL cases are characterized by the formation of hairpins ($\phi < 120^\circ$ and $\phi > 160^\circ$) for short initial evolution times. An example is shown at $T = 1$ in Fig. 3(b) for $\lambda = 0.5$ and $\phi = 90^\circ$. Nevertheless, at later times, as the disturbance elongates along the outlet asymptote, the regions of spanwise vorticity corresponding to the heads of the hairpins break and eventually only the legs (CVPs) remain. For values of ϕ in the range $120^\circ < \phi < 160^\circ$ vortex loops are observed for short initial evolution times. An example for $\lambda = 0.5$ and $\phi = 150^\circ$ is presented in Fig. 3(c) ($T = 1$). The vortex loop spreads ($T = 2.5$) before finally breaking into CVPs at later time (not shown). The disturbances remain localized in the spanwise direction in all cases.

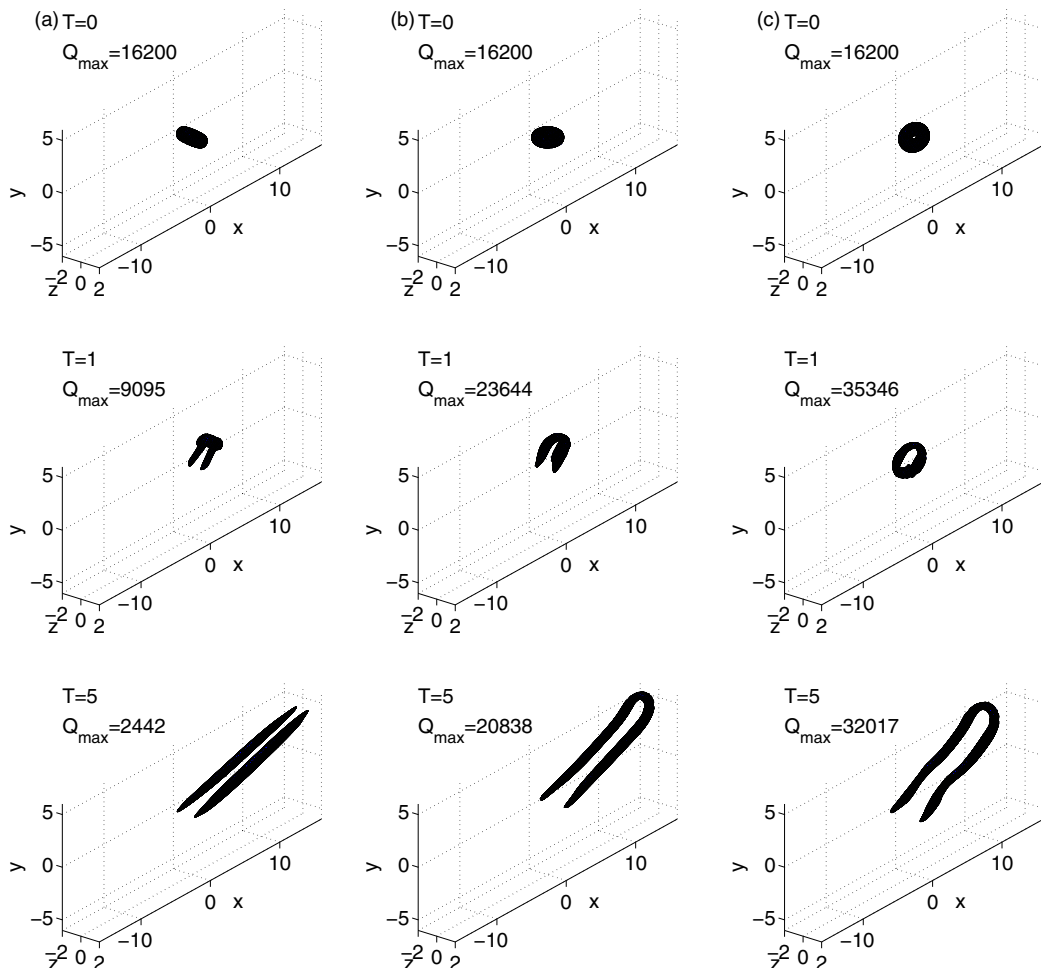


FIG. 4. Disturbance evolution for simple shear ($\lambda = 0$), $\varepsilon = 7.5$ (HNL), isosurfaces of $Q/Q_{\max} = 0.3$ for (a) $\phi = 50^\circ$, (b) $\phi = 90^\circ$, and (c) $\phi = 130^\circ$.

2. Simple shear

For the simple shear ($\lambda = 0$) the evolution features are similar to the ones observed for hyperbolic flows. For linear and MNL disturbances CVPs are formed and then they elongate and rotate towards the x axis [similarly to Fig. 3(a) above]. For HNL disturbances CVPs and hairpins are generated, depending on their initial orientation ϕ . Counterrotating vortex pairs are formed for $\phi < 80^\circ$, as shown in Fig. 4(a) for $\phi = 50^\circ$. The formation of CVPs is similar to the one described above for hyperbolic flows. Hairpins are formed for $\phi > 80^\circ$, as demonstrated in Fig. 4(b) for $\phi = 90^\circ$ and in Fig. 4(c) for $\phi = 130^\circ$. For $80^\circ < \phi < 130^\circ$ hairpins form rapidly [e.g., $T = 1$ in Fig. 4(b)], whereas for $\phi \geq 130^\circ$ the vortex loops spread and more time is required for the hairpins to form [e.g., Fig. 4(c)]. The above structures have been compared successfully with previous calculations obtained using FLUENT [17]. The disturbances remain localized in the spanwise direction in all cases, as in the case of hyperbolic flows.

To better understand the process of hairpin formation, the behavior of vortex lines, superimposed on the Q isosurfaces, has been investigated. The vortical structures of a CVP (for MNL disturbance and $\phi = 90^\circ$) and a hairpin (for HNL disturbance and $\phi = 90^\circ$) are presented in Fig. 5, together

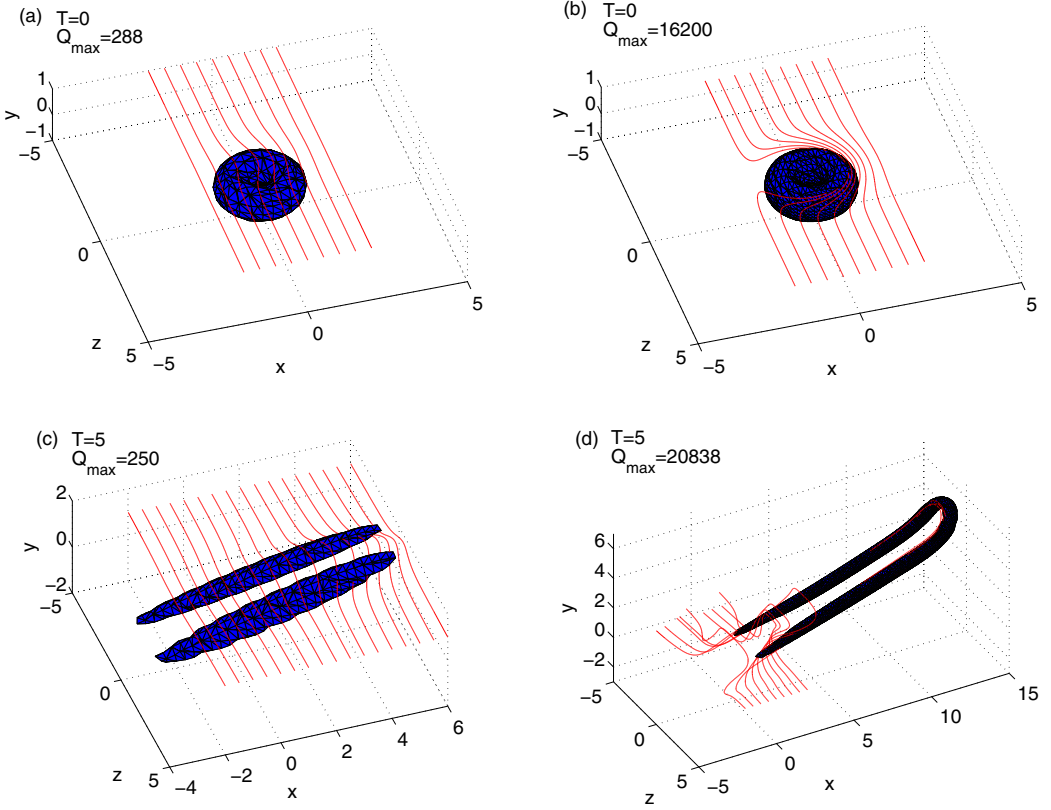


FIG. 5. Vortical structures (isosurfaces of $Q/Q_{\max} = 0.3$) for simple shear ($\lambda = 0$) and $\phi = 90^\circ$, together with the associated vortex lines indicated by the red color: (a) $\varepsilon = 1$ (MNL) and $T = 0$, (b) $\varepsilon = 7.5$ (HNL) and $T = 0$, (c) $\varepsilon = 1$ (MNL) and $T = 5$, and (d) $\varepsilon = 7.5$ (HNL) and $T = 5$.

with the associated vortex lines indicated by the red color. For the MNL disturbance [Fig. 5(a)] the vortex lines are not modified significantly and at $T = 5$ [Fig. 5(c)] they remain bent a little near the disturbance. On the other hand, for the HNL disturbance [Fig. 5(b)] the vortex lines near the disturbance bend significantly and at $T = 5$ [Fig. 5(d)] they become closely aligned with the hairpin legs and head. Thus, for the hairpin the vortex lines follow closely the Q isosurface.

3. Elliptic flows

For the elliptic flows ($\lambda < 0$) the disturbance evolution is similar for various values of λ except the limiting pure rotation case ($\lambda = -1$). The initial evolution phase ($T \lesssim 1$) is similar to the one described above for hyperbolic flows. For the linear and MNL disturbances CVPs are formed initially. An example of CVPs obtained at $T = 1$ is presented in Fig. 6(a) for $\lambda = -0.5$ and $\phi = 90^\circ$. At some later time (depending on λ and ϕ) two regions of localized vorticity are formed, as can be seen at $T = 20$ in Fig. 6(a). These regions intensify while being rotated by the base flow and the process continues. This scenario is general for all initial orientations; however, the exact shapes of the vortical structures depend on the initial orientation and differ from case to case. Unlike in the hyperbolic and simple shear flows, for elliptic flows the vortices spread in the spanwise direction.

For HNL disturbances hairpins and vortex rings are observed initially before breaking into various vortical structures. Several examples of hairpins that form by $T = 1$ are presented in Figs. 6(b)–6(d). In flows with small ellipticity (i.e., relatively high $|\lambda|$) the vortical structures give way to two growing regions of localized vorticity as in the linear and MNL cases. An example can be seen in Fig. 6(b)

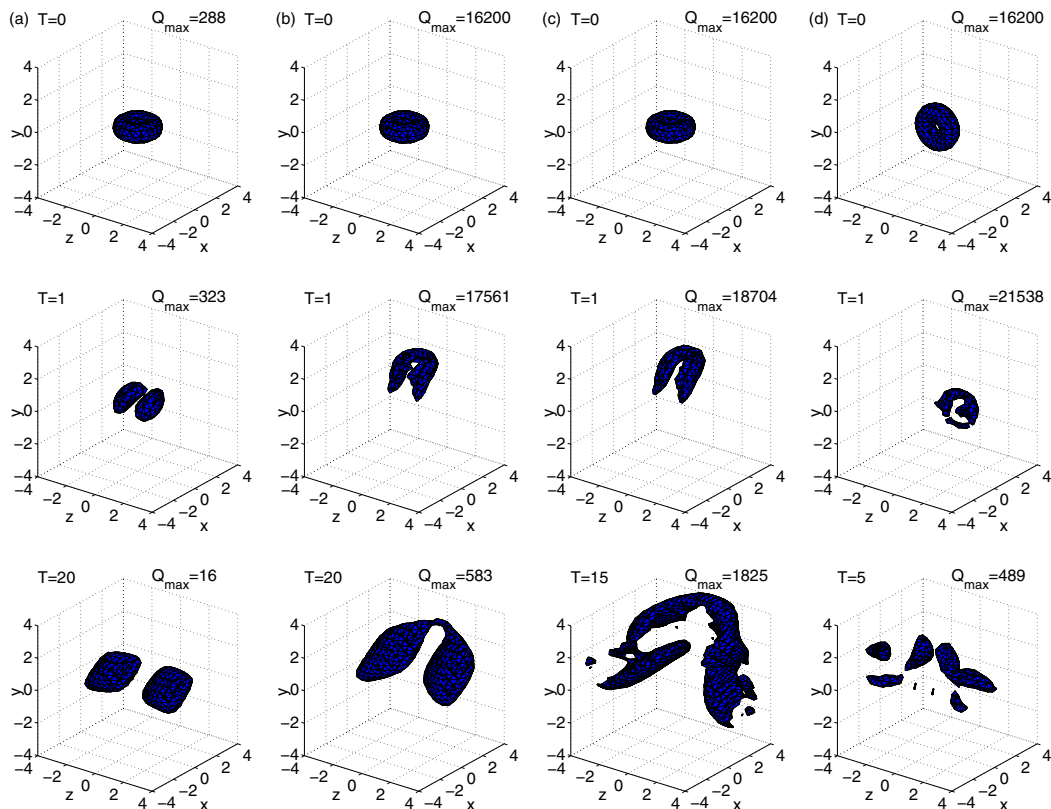


FIG. 6. Disturbance evolution in elliptic flows, isosurfaces of $Q/Q_{\max} = 0.3$ for (a) $\lambda = -0.5$, $\varepsilon = 1$ (MNL), and $\phi = 90^\circ$; (b) $\lambda = -0.5$, $\varepsilon = 7.5$ (HNL), and $\phi = 90^\circ$; (c) $\lambda = -0.25$, $\varepsilon = 7.5$ (HNL), and $\phi = 90^\circ$; and (d) $\lambda = -1$, $\varepsilon = 7.5$ (HNL), and $\phi = 0^\circ$.

for $\lambda = -0.5$ and $\phi = 90^\circ$, where two growing regions of localized vorticity appear similarly to the MNL case [Fig. 6(a)]. The two vorticity regions connect intermittently during the rotation cycle (e.g., at $T = 20$). In flows with highly elliptical streamlines (i.e., smaller $|\lambda|$) various vortical structures are observed, among which hairpin-shaped vortices appear and reappear during the cycle. An example is shown in Fig. 6(c) for $\lambda = -0.25$ and $\phi = 90^\circ$. Initially a hairpin is observed ($T = 1$), but later it breaks and a representative snapshot of an intermittent hairpin is presented at $T = 15$.

In pure rotation flow ($\lambda = -1$) the vortical structures eventually decay while spreading in the spanwise direction for all initial amplitudes. An example of the evolution of a HNL disturbance is presented in Fig. 6(d) for $\phi = 0^\circ$. Initially a hairpin begins to form ($T = 1$), but shortly afterward it breaks and the vortical structures spread along the spanwise direction ($T = 5$).

C. Integral properties

The total enstrophy, normalized by its initial value, as a function of time and initial vortex orientation is presented in Fig. 7 for $\lambda = 1$ (irrotational flow) and $\varepsilon = 1$ (MNL). In Fig. 7(a) the contours correspond to equally spaced isolines of the normalized enstrophy (with the symbol $+$ indicating the numerical values of the isolines). The horizontal axis corresponds to the time and the vertical axis to the initial vortex orientation angle ϕ . Red (solid) lines represent isolines where enstrophy is greater than its initial value, whereas blue (dotted) lines represent isolines where enstrophy is less than its initial value. It can be seen that for $\phi = 120^\circ$ the enstrophy grows monotonically, whereas for $\phi = 30^\circ$ it decays initially but starts to grow and returns to its initial

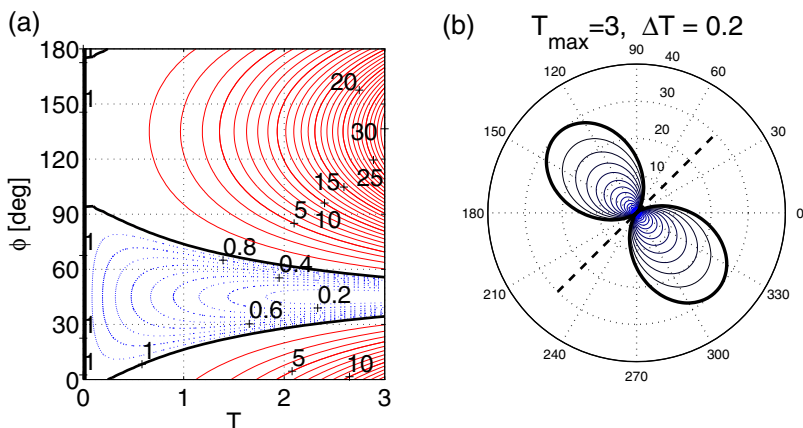


FIG. 7. Total normalized enstrophy as a function of time and initial vortex orientation for $\lambda = 1$ (irrotational flow) and $\varepsilon = 1$ (MNL): (a) enstrophy contours vs time (horizontal) and initial vortex orientation angle (vertical) and (b) enstrophy (radial coordinate) vs initial vortex orientation angle ϕ (angular coordinate). Temporal spacing between the contours is indicated above the figure.

value by $T \approx 2.3$. The region of ϕ corresponding to decay shrinks with time, whereas the region corresponding to growth expands. The optimal initial orientation angle for which the growth is maximal is around $\phi = 135^\circ$, corresponding to $W/W(0) = 30$.

A different presentation of the normalized enstrophy is shown in Fig. 7(b), where the radial coordinate represents the normalized enstrophy and the angular coordinate represents ϕ . The contours correspond to different evolution times with the initial contour being the unit circle marked by a thick blue line and the final contour, corresponding to T_{\max} , marked by a thick black line. The outlet asymptote is marked by the dashed line. Figure 7(a) is more adequate for understanding the temporal evolution of the total enstrophy, whereas Fig. 7(b) is more convenient for finding the optimal initial orientation. As can be seen in Fig. 7(b), the optimal initial orientation is around $\phi = 135^\circ$, which achieves a radius of 30 at $T_{\max} = 3$. An important conclusion from Fig. 7(b) is that the most significant amplification occurs for vortices having the initial orientation of μ perpendicular to the outlet asymptote ($\phi = 135^\circ$) and that the least amplified disturbances have the orientation of μ in the direction of the outlet asymptote ($\phi = 45^\circ$). This observation can be explained from the linear instability of hyperbolic flows to plane waves [26]. It has been found that for the unstable waves in inviscid flow, the vorticity component in the outlet direction grows exponentially, while the vorticity component in the direction normal to outlet decays exponentially. The mechanism responsible for the growth is the vortex stretching mechanism. When the Gaussian vortex is oriented with μ close to being perpendicular to the outlet ($\phi \approx 135^\circ$) it has significant initial vorticity along the outlet, which leads to rapid growth. On the other hand, when the Gaussian vortex is oriented with μ close to being along the outlet ($\phi \approx 45^\circ$) it has very small or zero initial vorticity along the outlet, leading to initial decay and delay of the growth stage.

The normalized enstrophy for other hyperbolic base flows and simple shear is presented in Fig. 8 and for elliptic flows in Fig. 9. The presentation method is the same as in Fig. 7. The outlet asymptote for hyperbolic flows is marked by the dashed lines. The enstrophy evolution is very similar for the linear and MNL cases, thus only the MNL (first and second columns) and HNL (third and fourth columns) cases are presented.

The evolution of the total enstrophy for all hyperbolic flows [$\lambda > 0$, Figs. 8(a)–8(c)] is qualitatively similar to the irrotational case presented above ($\lambda = 1$, Fig. 7). For all hyperbolic flows the region of ϕ corresponding to decay shrinks with time, whereas the region corresponding to growth expands. It can be seen that the most significant amplification occurs for vortices with initial orientation in the range $120^\circ < \phi < 150^\circ$, i.e., the vortices having the vortex plane initially aligned with the outlet

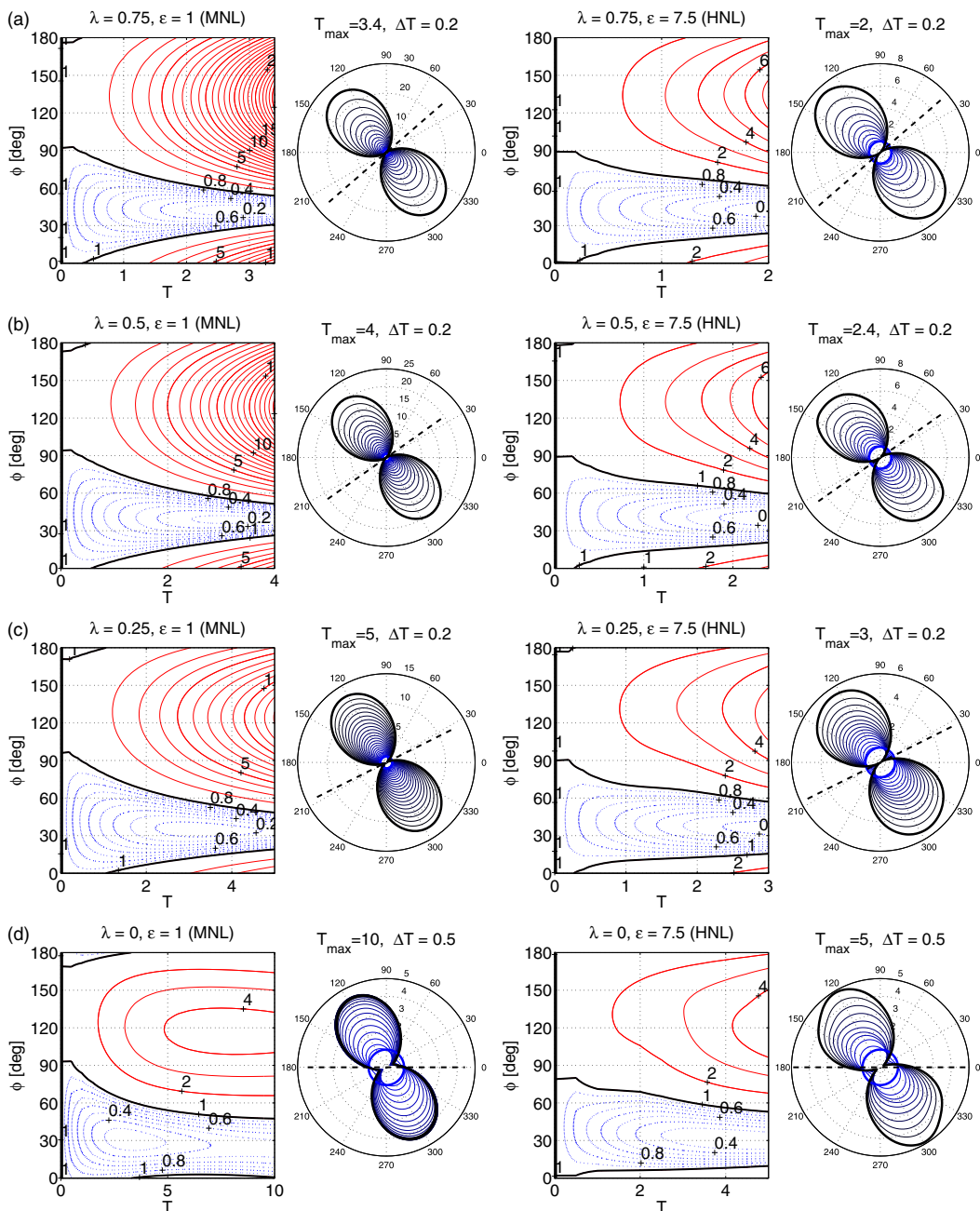


FIG. 8. Total normalized enstrophy as a function of time and initial vortex orientation for hyperbolic flows and simple shear. The plotting method is the same as in Fig. 7. The first and second columns show the MNL case ($\epsilon = 1$) and the third and fourth columns the HNL case ($\epsilon = 7.5$) for (a) $\lambda = 0.75$, (b) $\lambda = 0.5$, (c) $\lambda = 0.25$, and (d) $\lambda = 0$.

(the vortex plane is initially perpendicular to the orientation of μ). These vortices are preferred since they contain significant initial vorticity along the outlet, which grows according to a linear instability mechanism [26]. The least amplified disturbances contain the smallest initial vorticity

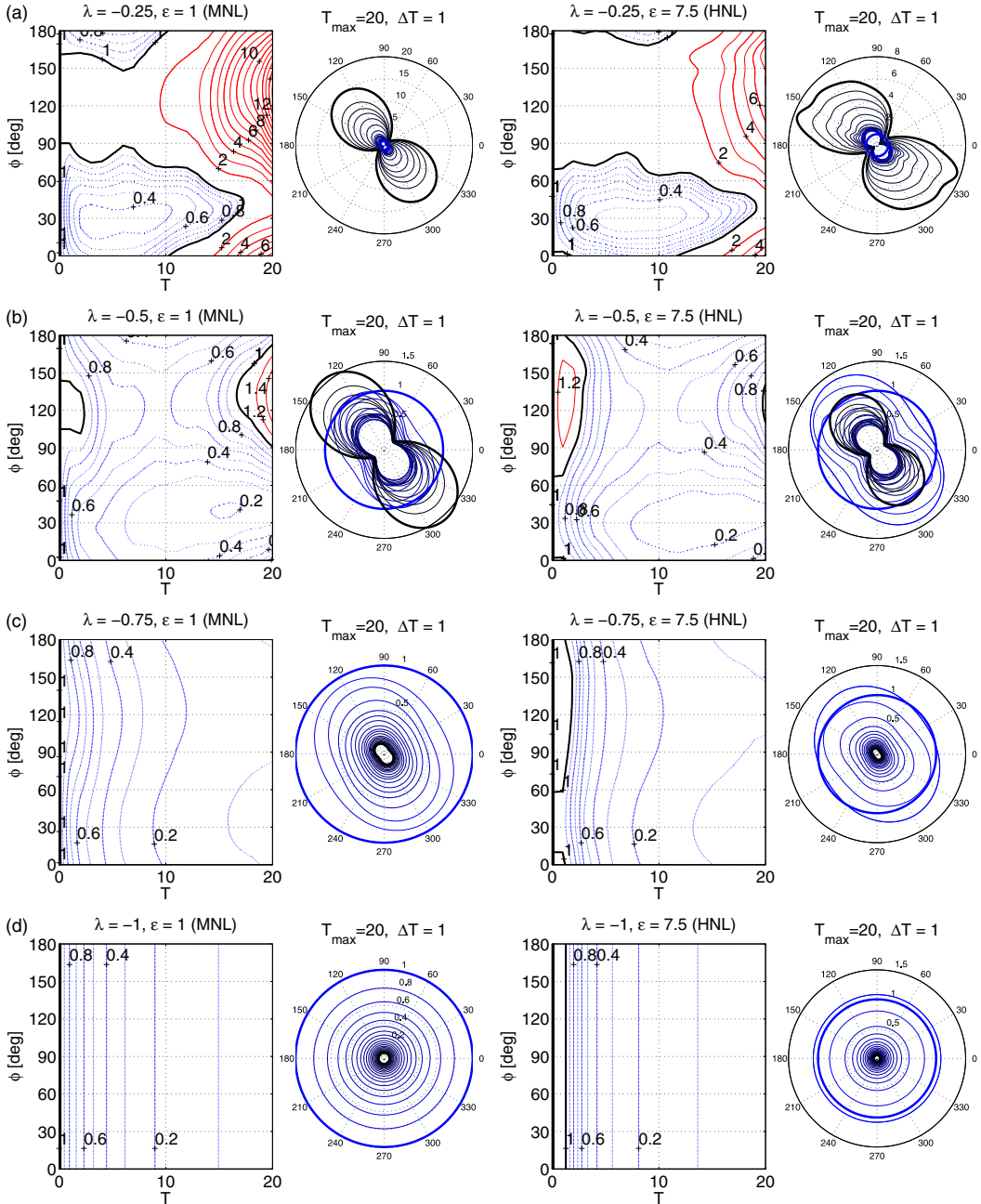


FIG. 9. Total normalized enstrophy as a function of time and initial vortex orientation for elliptic flows. The plotting method is the same as in Fig. 7. The first and second columns show the MNL case ($\epsilon = 1$) and the third and fourth columns the HNL case ($\epsilon = 7.5$) for (a) $\lambda = -0.25$, (b) $\lambda = -0.5$, (c) $\lambda = -0.75$, and (d) $\lambda = -1$.

along the outlet, which results in initial decay and delay of the growth stage. The enstrophy growth is linked to the growth of the vorticity component along the outlet direction, due to vortex stretching, for all unstable waves in the Gaussian vortex. The enstrophy growth rate is not constant, since the

growth rate of individual plane waves depends on time, wavelength, and wave-vector orientation. Nevertheless, in the linear case it is possible to obtain an asymptotic analytical expression for the enstrophy, which at long times behaves as $W(t) \sim \exp(\kappa t)/(\kappa t)^{3/2}$. Further analytical expressions for the asymptotic behavior of the enstrophy in the linear case, associated with other time scales of the problem, are provided in Appendix B. The vortical structures corresponding to the enstrophy growth are CVPs, such as the ones shown in Fig. 3, which contain mostly vorticity along the outlet asymptote. Nonlinearity has a small effect on the optimal amplification.

For simple shear [Fig. 8(d)] the enstrophy undergoes transient growth. For example, for $\phi = 150^\circ$ the maximum is reached at $T \approx 7$ after which slow decay begins. The optimal initial orientation is approaching $\phi = 120^\circ$ at long times for both linear and nonlinear disturbances. This flow can be considered as a limiting case of hyperbolic flows, except that the growth in this case is transient only. The effect of nonlinearity is a small enhancement of the growth with little effect on the optimal amplification.

For elliptic flows ($\lambda < 0$, Fig. 9) there are regions of initial growth and decay similarly to the hyperbolic flows. For example, in Fig. 9(a) for $\phi = 40^\circ$ the enstrophy decays initially but then begins to grow and returns to its initial value at $T \approx 17$. It is known that arbitrary elliptical flows are linearly unstable [27,28]. The enstrophy growth is linked to the growth of all unstable plane waves in the Gaussian vortex. The enstrophy growth rate is not constant, since the growth rate of individual plane waves depends on time, wavelength, and wave-vector orientation. The vortical structures corresponding to the enstrophy growth are the two regions of localized vorticity, such as the ones shown in Fig. 6(a), which grow in magnitude and change their shape periodically. As the base-flow streamlines become less elliptic ($\lambda \rightarrow -1$) the growth stage is delayed and begins at later times so that no growth may be seen when we are limited to a finite observation time. For example, for $\lambda = -0.5$ [Fig. 9(b)] the growth stage begins at $T \approx 10$ for $\phi = 130^\circ$ and $T \approx 17$ for $\phi = 40^\circ$, whereas for $\lambda = -0.75$ [Fig. 9(c)] no growth is observed up to $T = 20$. Although for any $\lambda > -1$ the growth stage will begin eventually, in the limiting case of pure rotation flow [$\lambda = -1$, Fig. 9(d)] the disturbance ultimately decays. For the linear and MNL cases the most significant amplification occurs for vortices with initial orientation in the range $120^\circ < \phi < 130^\circ$. In flows with highly elliptical streamlines [e.g., Fig. 9(a) for $\lambda = -0.25$] the optimal initial orientation for HNL disturbances changes from $\phi = 120^\circ$ for short times to $\phi = 160^\circ$ at later times and the contour pattern is irregular. For flows with smaller ellipticity [see, e.g., Figs. 9(b) and 9(c) for $\lambda = -0.5$ and $\lambda = -0.75$, respectively] the enstrophy in the HNL cases behaves similarly to the linear and MNL cases.

The vortex inclination angle α as a function of time is shown in Fig. 10 for various base flows. The radial coordinate represents the time (shifted by one, so the unit circle corresponds to $T = 0$) and each curve corresponds to a different initial vortex orientation ϕ . The outlet asymptote for hyperbolic flows is marked by the dashed lines. Only the MNL and HNL cases are presented as in previous plots. Note that there is a 90° difference between the initial inclination angle $\alpha(T = 0)$ and the initial orientation angle ϕ . Thus, for example, in Fig. 10(a) the curve that begins on the unit circle with $\alpha = 90^\circ$ and then monotonically decreases to $\alpha = 45^\circ$ at long times corresponds to $\phi = 0^\circ$ (represented by the thick purple line for demonstration purposes), whereas the curve that begins with $\alpha = 150^\circ$ and then monotonically increases to $\alpha = 225^\circ$ corresponds to $\phi = 60^\circ$ (represented by the thick blue line for demonstration purposes). Vortices with initial values of α in the interval $-45^\circ < \alpha < 135^\circ$ are rotated towards $\alpha = 45^\circ$, whereas other vortices are rotated towards $\alpha = 225^\circ$. It should be noted that, due to the symmetry of the base flow, the angles 45° and 225° correspond to the same vortex inclination angle as the evolution of disturbances with initial angles of ϕ and $\phi + 180^\circ$ is identical up to a rotation of 180° . For the hyperbolic flows [$\lambda > 0$, Figs. 10(a)–10(d)] all vortices change their vortex inclination angles and eventually have their vortex planes aligned with the outlet asymptote. The initial change in α is faster for the HNL cases due to the symmetry breaking. For example, for $\lambda = 1$ and the MNL case [Fig. 10(a)] most of the rotation occurs up to $T = 1$ before settling on the asymptote, whereas for the HNL case most of the rotation occurs up to $T = 0.5$. However, for long times more scattering is observed for the HNL case for which the settling down phase to the asymptotic value is slower (compare the MNL case to the HNL

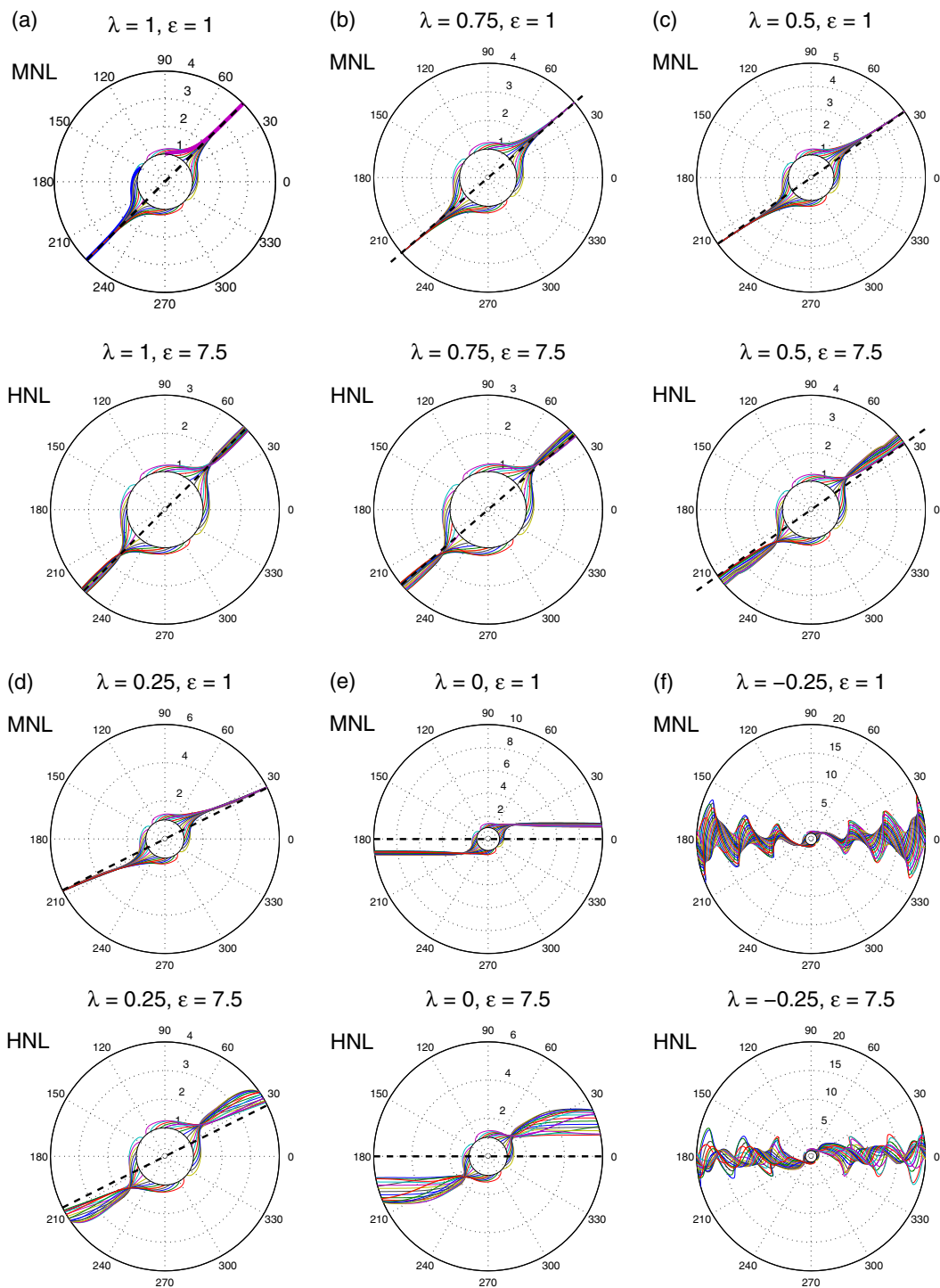


FIG. 10. Vortex inclination angle α vs time for various flows: (a) $\lambda = 1$, (b) $\lambda = 0.75$, (c) $\lambda = 0.5$, (d) $\lambda = 0.25$, (e) $\lambda = 0$, (f) $\lambda = -0.25$, (g) $\lambda = -0.5$, (h) $\lambda = -0.75$, and (i) $\lambda = -1$ (only $\phi = 0^\circ, 180^\circ$ are shown). Odd rows show the MNL case ($\epsilon = 1$) and even rows the HNL case ($\epsilon = 7.5$). The radial coordinate represents the shifted time $1 + T$.

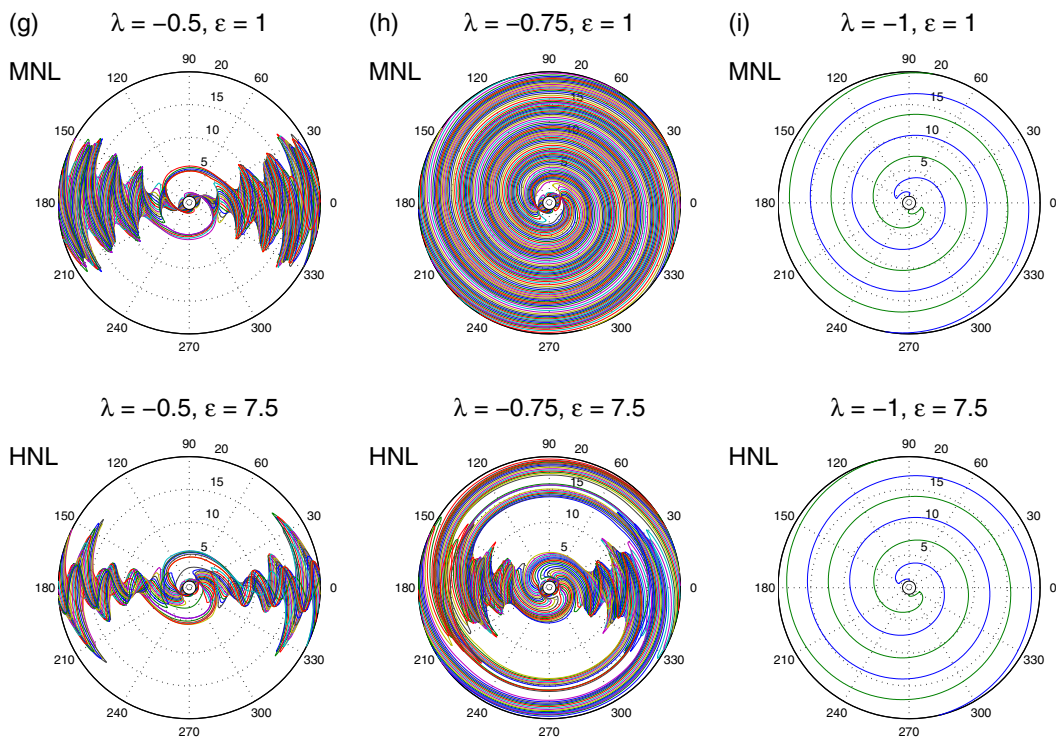


FIG. 10. (Continued.)

one at $T > 1$). As the flow tends to simple shear (i.e., $\lambda \rightarrow +0$) the asymmetry of the curves $\alpha(t)$ with respect to the asymptotic (outlet) direction becomes stronger, so all curves approach the outlet from above (in the first quadrant) and from below (in the third quadrant). For the simple shear case [Fig. 10(e)] the vortex angle tends towards zero, i.e., the vortices tend towards extension along the x axis. The trend towards the x axis is much slower for HNL disturbances.

For elliptic flows [Figs. 10(f)–10(h)] the angle becomes periodic with half the period of the base flow ($T_{\text{ell}} = 2\pi/\eta$). Such periodicity arises due to the symmetry of the base flow and has been observed previously in the linear case [20]. The periodicity of the angle is linked to the formation of two regions of localized vorticity, which grow in magnitude and change their shape periodically. The amplitude of the oscillation for the MNL case is bigger than for the HNL case. The amplitude also becomes bigger as the streamlines become less elliptic ($\lambda \rightarrow -1$). For $\lambda = -0.75$ [Fig. 10(h)] the amplitude in the MNL case exceeds 90° , so spirals are observed. For the pure rotation case [Fig. 10(i)] only $\phi = 0^\circ$ and $\phi = 180^\circ$ are shown. A temporal period of 2π (as in this case $\eta = \frac{1}{2}|\Omega| = \Omega_*$) can be seen and the differences between the MNL and HNL cases are small.

Next we follow the evolution of a specific disturbance in various base flows. A disturbance with initial orientation $\phi = 120^\circ$ is selected as a representative disturbance in the range of the most amplified disturbances. The strength of the vortex for various base flows is presented in Fig. 11 for MNL [Fig. 11(a)] and HNL [Fig. 11(b)] disturbances, with the linear evolution (calculated analytically [19,20,22]) given by the dashed lines. It can be seen that there are minor differences between the MNL and the linear cases and that as λ is higher the disturbance grows more rapidly. The main differences between the MNL [Fig. 11(a)] and HNL [Fig. 11(b)] cases are observed at the initial stage ($T < 2$) in which the HNL disturbances undergo significant amplification. In particular, note the bottom two curves for $\lambda = -1$ and $\lambda = -0.75$, where small transient growth is observed at short times. It should be noted that transient growth usually refers to linear mechanisms, associated with linearly stable flows (or subcritical transition). However, the transient growth observed in the

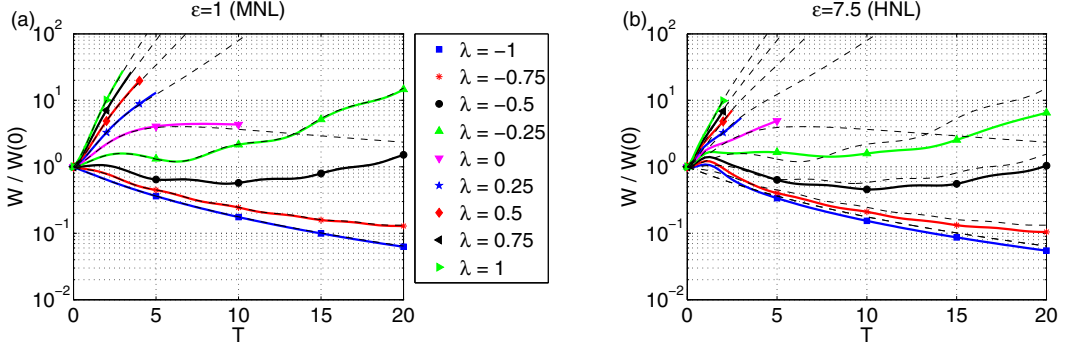


FIG. 11. Total enstrophy vs time of a disturbance with initial orientation $\phi = 120^\circ$ embedded in various base flows for (a) $\varepsilon = 1$ (MNL) and (b) $\varepsilon = 7.5$ (HNL). The linear evolution is given by the dashed lines.

HNL case is linked to nonlinear interactions between the waves composing the Gaussian vortex packet, which result in self-induced motion of the vortex. The nonlinear self-induced motion is mostly dominant at short times when the vortex is more localized. For hyperbolic flows the effect of nonlinearity at long times is not significant, as can be observed by comparing the solid lines (HNL) with the linear behavior given by the dashed lines. For elliptic flows the differences observed at long times are due to the initial self-induced motion and they can be approximated by an almost constant shift relative to the linear case.

The CVS for several base flows is shown in Fig. 12 for various initial amplitudes and initial disturbance orientations of $\phi = 0^\circ, 60^\circ, 120^\circ$, and 180° . The vortices are initially positioned at the origin and the time step between two consecutive symbols is equal. In the linear case the vortex remains in the origin as no self-induced motion occurs. For the MNL case little self-induced motion occurs, followed by convection of the CVS by the base flow. However, the nonlinear self-induced motion in the MNL case has a negligible effect on the overall development of the vortex. In the HNL case, the vortex initially propels itself in the direction of its orientation and then continues to progress due to self-induced motion and convection by the base flow. The self-induced motion is more dominant at the initial times when the vortex is more localized. For hyperbolic flows [Figs. 12(a) and 12(b)] the CVS is eventually convected by the base flow along the outlet asymptote (except the linear case), whereas for simple shear [Fig. 12(c)] it is convected by the base flow and gradually approaches the base-flow direction (x axis). For elliptic flows [Fig. 12(d)] the CVS achieves the farthest distance from the origin during the initial self-induced motion and then it approaches an approximately elliptic path. For the pure rotation flow [Fig. 12(e)] only $\phi = 0^\circ$ is presented and the CVS gradually moves farther away from the origin.

IV. CONCLUSION

The evolution of localized disturbances has been investigated in various homogeneous shear base flows of the form $\mathbf{V} = (-\frac{1}{2}(\Omega + \sigma)y, -\frac{1}{2}(\sigma - \Omega)x, 0)$, where σ and Ω are the strain rate and vorticity of the base flow, respectively. Coherent structures have been obtained for hyperbolic and simple shear flows, i.e., $\lambda \equiv (\sigma - \Omega)/(\sigma + \Omega) \geq 0$. Counterrotating vortex pairs form in the linear and moderately nonlinear cases for hyperbolic and simple shear flows. The dominance of shear over rotation ($|\sigma| > |\Omega|$) leads to elongation of the localized disturbance along the outlet asymptote (x axis for simple shear). For the highly nonlinear disturbance CVPs form for hyperbolic flows as the base flow succeeds in breaking the heads (spanwise vorticity) of the hairpins. For simple shear the heads remain and hairpin vortices are observed even at long times. For elliptical base flows CVPs, hairpins and vortex loops form initially, however they do not last and break into various vortical structures that spread in the spanwise direction. Except for HNL disturbances and small values of

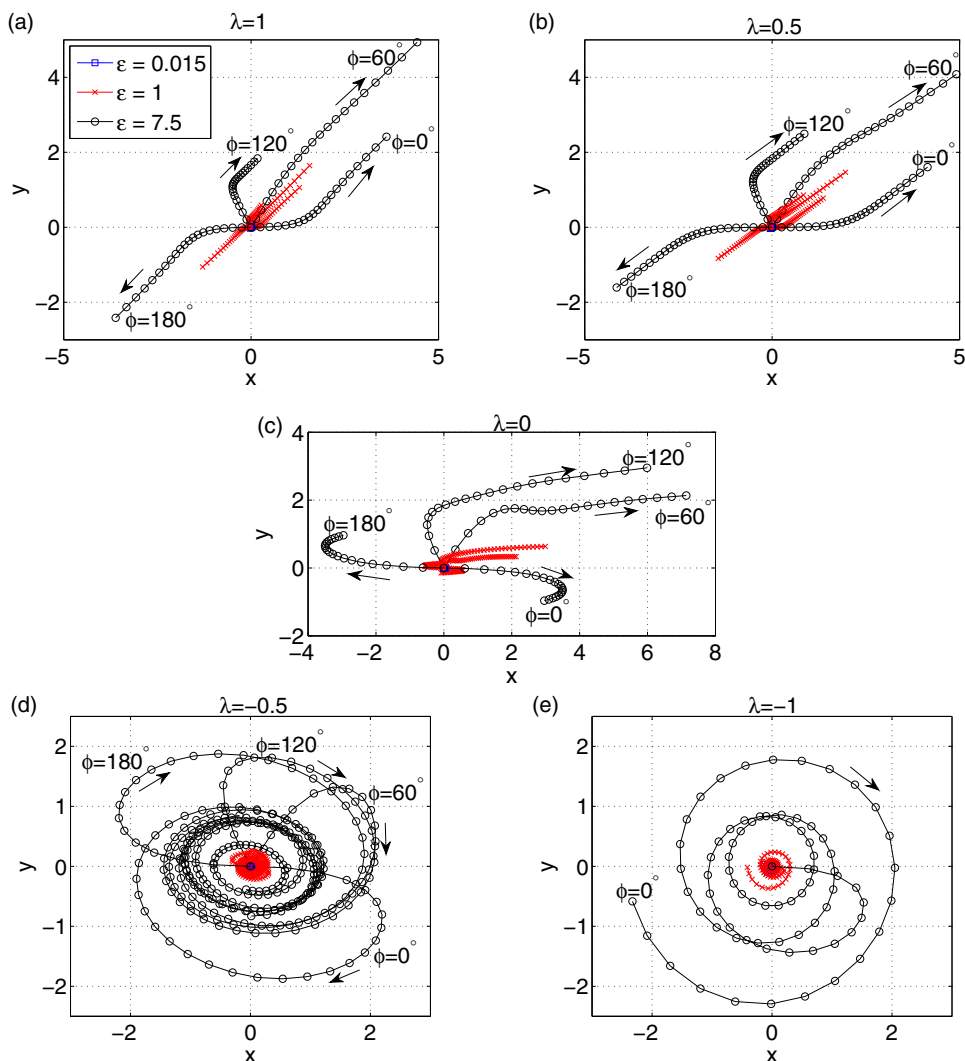


FIG. 12. Center of the vortical structure on the x - y plane for initial orientations $\phi = 0^\circ, 60^\circ, 120^\circ, 180^\circ$ and initial magnitudes $\varepsilon = 0.015, 1, 7.5$ for (a) $\lambda = 1$, (b) $\lambda = 0.5$, (c) $\lambda = 0$, (d) $\lambda = -0.5$, and (e) $\lambda = -1$ (only $\phi = 0^\circ$ is shown). The time step between two consecutive symbols is equal and the arrows indicate the direction of increasing time.

$|\lambda|$, the enstrophy growth is governed by a linear mechanism, preceded by a transient behavior. In this mechanism two localized regions of vorticity form and intensify while being rotated by the base flow and the process continues. For HNL disturbances embedded in highly elliptical base flows (having small values of $|\lambda|$) various vortical structures are observed, among which hairpin-shaped vortices appear intermittently during the cycle. A major difference between the vortex evolution in hyperbolic and elliptic flows is that in hyperbolic flows the vortex remains localized in the spanwise direction, whereas in elliptic flows it spreads along the spanwise direction.

The most efficient (in terms of formation time and growth) mechanism for the formation of CVPs is obtained for irrotational flow ($\lambda = 1$), whereas the most efficient mechanism for formation of hairpins is for simple shear ($\lambda = 0$). Elliptic flows, on the other hand, do not seem adequate for obtaining the evolution of such coherent structures. The most significant amplification occurs for

TABLE I. Summary of the numerical parameters used in the study.

Base flow	σ (s ⁻¹)	Ω (s ⁻¹)	ε	x_f	y_f	z_f	N_x	N_y	N_z	$(\Delta t)_0/\Delta t$	T_{\max}
1	-80	0	0.015,1	16	16	8	128	128	64	40	3
	-80	0	7.5	16	16	8	256	256	64	20	2
2	-70	-10	0.015,1	16	16	8	128	128	64	40	3.5
	-70	-10	7.5	16	16	8	256	256	64	20	2
3	-60	-20	0.015,1	16	12	8	100	80	64	20	4
	-60	-20	7.5	16	12	8	200	150	64	10	2.5
4	-50	-30	0.015,1	20	10	8	128	64	64	10	5
	-50	-30	7.5	20	10	8	256	128	64	10	3
5	-40	-40	0.015,1	25	8	10	160	64	64	10	10
	-40	-40	7.5	25	8	10	320	128	64	20	5
6	-30	-50	0.015,1,7.5	20	10	20	128	64	128	10	20
7	-20	-60	0.015,1,7.5	20	10	20	128	64	128	10	20
8	-10	-70	0.015,1,7.5	20	20	20	128	128	128	10	20
9	0	-80	0.015,1,7.5	20	20	20	128	128	128	10	20

vortices with initial orientation in the range $120^\circ < \phi < 150^\circ$ as these vortices contain significant initial vorticity along the outlet asymptote for hyperbolic flows. The vorticity along the outlet asymptote grows due to vortex stretching according to a linear instability mechanism [26].

The effect of moderate nonlinearity on the integral properties is minor and although symmetry breaking occurs (due to self-induced motion), the overall evolution is very similar to the linear case. On the other hand, the evolution of HNL disturbances is rather different. At short times considerable self-induced motion occurs, accompanied by significant growth. At later times the evolution in the HNL and linear cases is similar up to a constant enstrophy shift. The enstrophy is unbounded for hyperbolic and elliptic flows (except $\lambda = -1$) and only transient for the limiting cases of simple shear ($\lambda = 0$) and pure rotation flow ($\lambda = -1$).

Finally, a comment regarding the analytical-based method is in order. It can be utilized to calculate the evolution of any localized disturbance, not necessarily the Gaussian vortex chosen in this study. The method is also capable of following the evolution of nonlocalized periodic disturbances (see, e.g., [25]).

ACKNOWLEDGMENT

This research was supported by the Israeli Science Foundation (Grant No. 1394/11) and Russian Science Support Foundation (Grant No. 14-05-00080).

APPENDIX A: NUMERICAL PARAMETERS

This Appendix summarizes the numerical parameters used in the study. The numerical parameters are the normalized dimensions of the computational domain (x_f, y_f, z_f) , the number of points $N = (N_x, N_y, N_z)$, the time step [as a fraction of the default time step $(\Delta t)_0 = 0.000625$ s], and the final (maximal) normalized time T_{\max} . For each base flow σ and Ω and initial vortex strength ε the numerical parameters are given in Table I. The computational domain varies for different base flows because in some cases the disturbance remains localized in a certain region within the domain, so it has been possible to reduce the domain size without affecting the evolution of the disturbance. Convergence has been verified by obtaining negligible differences in the evolution as a result of doubling the computational domain size for a fixed cell size and doubling the number of points in each direction for a fixed domain (i.e., fixed domain with half-cell size). Differences of up to 2% in the integral quantities have been obtained. An example of a convergence test for simple shear, HNL disturbance, and $\phi = 90^\circ$ is presented in Fig. 13. Results for the base calculation are indicated by

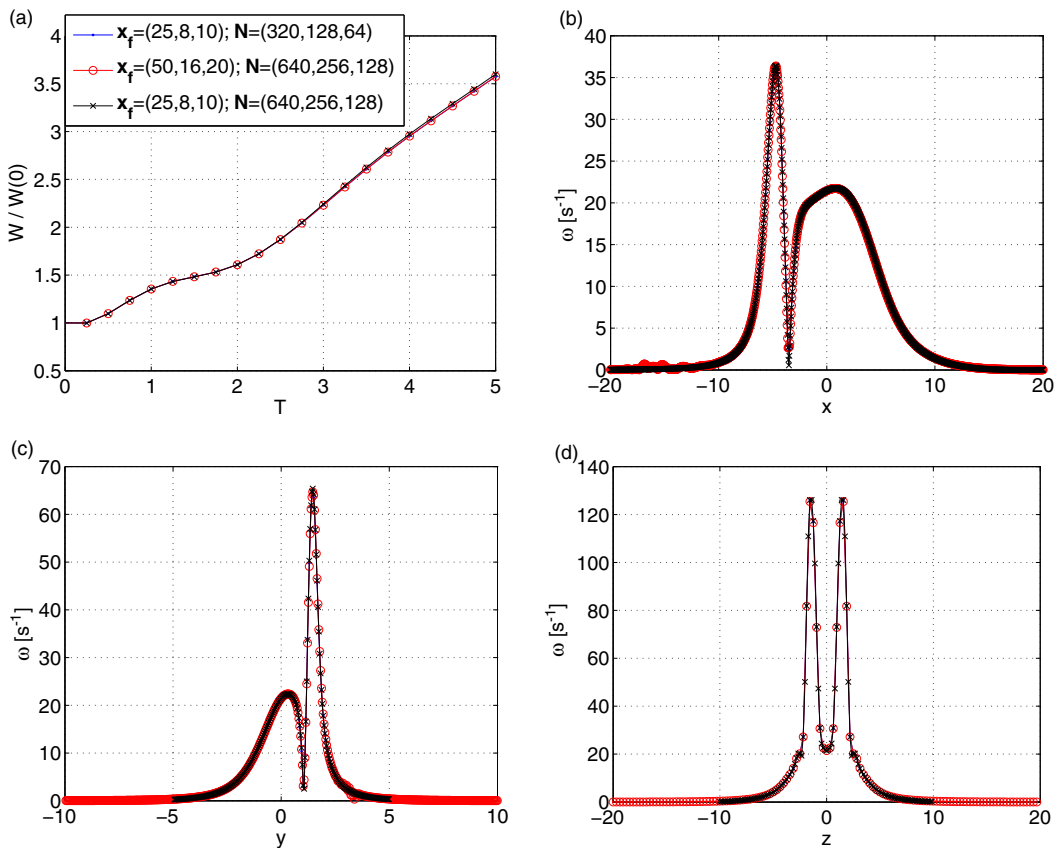


FIG. 13. Convergence test for simple shear ($\lambda = 0$), HNL ($\varepsilon = 7.5$), and $\phi = 90^\circ$. Shown is a comparison between the base calculation (blue dots), double domain with fixed cell size (red circles), and fixed domain with half-cell size (black crosses) for (a) the evolution of enstrophy and (b)–(d) the axial distribution of vorticity magnitude ($\omega = |\omega|$) at $T = 5$.

the blue dots, for the double domain with fixed cell size by the red circles, and for the fixed domain with half-cell size (double number of points in each direction) by the black crosses. The enstrophy is presented in Fig. 13(a) and the distribution of vorticity magnitude at $T = 5$ along x , y , and z is shown in Figs. 13(b)–13(d), respectively. Excellent agreement is seen in all cases.

APPENDIX B: LINEAR EVOLUTION OF VORTICAL DISTURBANCES IN HYPERBOLIC FLOW: ANALYTICAL RESULTS

In this Appendix we present analytical results concerning the linear evolution of the total enstrophy in hyperbolic flows. The final expressions are exact for irrotational flow and approximate for arbitrary hyperbolic flows. The goal is to fix an inadvertence made in Ref. [19] that led to incorrect results concerning the asymptotical behavior of enstrophy at large times. The total enstrophy for hyperbolic flows is unbounded, rather than viscous decay [as was shown in Figs. 3 and 4(b) in Ref. [19]]. Although the analytical expressions in Ref. [19] are correct, the long-time evolution of the total enstrophy for the viscous case was calculated (numerically) improperly. The error is due to an insufficiently small integration step in the numerical integration over the azimuthal angle in Fourier space, required at large times. At large times the disturbance is increasingly compressed around the inlet direction in \mathbf{k} space, which requires a corresponding reduction of the integration step.

For *irrotational flow* ($\lambda = 1$) the analytical integral expressions for the enstrophy [19] can be simplified to exact analytical expressions. The normalized enstrophy is given by

$$W(t) = \frac{1}{2} \frac{1}{D_1 D_2 D_3} \left[e^{2\kappa t} \sin^2 \left(\phi + \frac{1}{4} \pi \right) \left(\frac{1}{D_1^2} + \frac{1}{D_3^2} \right) + e^{-2\kappa t} \sin^2 \left(\phi - \frac{1}{4} \pi \right) \left(\frac{1}{D_2^2} + \frac{1}{D_3^2} \right) \right], \quad (\text{B1})$$

where the length scales D_1 , D_2 , and D_3 are given by

$$D_1 = e^{\kappa t} \sqrt{1 + \frac{2}{\text{Re}}(1 - e^{-2\kappa t})}, \quad D_2 = e^{-\kappa t} \sqrt{1 + \frac{2}{\text{Re}}(e^{2\kappa t} - 1)}, \quad D_3 = \sqrt{1 + \frac{4\kappa t}{\text{Re}}}. \quad (\text{B2})$$

In the inviscid case the exact expression reduces to

$$W(t) = \frac{1}{2} \left[\sin^2 \left(\phi + \frac{1}{4} \pi \right) (1 + e^{2\kappa t}) + \sin^2 \left(\phi - \frac{1}{4} \pi \right) (1 + e^{-2\kappa t}) \right]. \quad (\text{B3})$$

For *arbitrary hyperbolic flows* ($0 < \lambda < 1$) the exact analytical expressions are given only in integral form [19]. Nevertheless, asymptotical expressions can be obtained. The normalized enstrophy is given by

$$W(t) \approx \frac{1}{2} \sin^2(\psi + \phi) \frac{e^{2\kappa t}}{H_1 H_2 H_3^3}, \quad (\text{B4})$$

where the length scales H_1 , H_2 , and H_3 are given by

$$H_1 = \sqrt{1 + \frac{(1 + \lambda)^2}{2\lambda^{3/2}\text{Re}} e^{2\kappa t}}, \quad H_2 \approx \sqrt{1 + \frac{2}{\lambda^{1/2}\text{Re}}}, \quad H_3 = \sqrt{1 + \frac{4\kappa t}{\lambda^{1/2}\text{Re}}}. \quad (\text{B5})$$

The asymptotic expressions for H_1 , H_2 , and H_3 for the most interesting case $\text{Re} \gg 1$ are given by

$$H_1 \approx \begin{cases} 1, & \kappa t \ll \tau_1 \\ \frac{(1+\lambda)e^{\kappa t}}{\sqrt{2\text{Re}\lambda^{3/4}}}, & \kappa t \gg \tau_1, \end{cases} \quad H_2 \approx 1, \quad H_3 \approx \begin{cases} 1, & \kappa t \ll \tau_2 \\ \frac{2(\kappa t)^{1/2}}{\lambda^{1/4}\text{Re}^{1/2}}, & \kappa t \gg \tau_2, \end{cases} \quad (\text{B6})$$

where we have defined

$$\tau_1 = \frac{1}{2} \ln \left[\frac{2\lambda^{3/2}\text{Re}}{(1 + \lambda)^2} \right], \quad \tau_2 = \frac{1}{4} \lambda^{1/2} \text{Re}. \quad (\text{B7})$$

Now we can distinguish between three types of asymptotical behavior in three different time intervals: (I) In the initial (inviscid) stage ($1 \ll \kappa t \ll \tau_1$),

$$H_1 \approx H_2 \approx H_3 \approx 1, \quad (\text{B8})$$

$$W_{\text{I}}(t) \approx \left[\frac{1}{2} \sin^2(\psi + \phi) \right] e^{2\kappa t}; \quad (\text{B9})$$

(II) in the intermediate stage ($1 \ll \tau_1 \ll \kappa t \ll \tau_2$),

$$H_1 \approx (2\lambda^{1/2}\text{Re})^{-1/2} (\sigma/\kappa) e^{\kappa t}, \quad H_2 \approx H_3 \approx 1, \quad (\text{B10})$$

$$W_{\text{II}}(t) \approx \left[\frac{\kappa \lambda^{1/4}}{\sigma} \sqrt{\text{Re}/2} \sin^2(\psi + \phi) \right] e^{\kappa t}; \quad (\text{B11})$$

and (III) in the final stage ($1 \ll \tau_1 \ll \tau_2 \ll \kappa t < \infty$),

$$H_1 \approx (2\lambda^{1/2}\text{Re})^{-1/2} (\sigma/\kappa) e^{\kappa t}, \quad H_2 \approx 1, \quad H_3 \approx 2(\kappa t)^{1/2} / \lambda^{1/4} \text{Re}^{1/2}, \quad (\text{B12})$$

$$W_{\text{III}}(t) \approx \left[\frac{(\text{Re})^2 \lambda \kappa}{8\sqrt{2}} \frac{\sin^2(\psi + \phi)}{\sigma} \right] \frac{e^{\kappa t}}{(\kappa t)^{3/2}}. \quad (\text{B13})$$

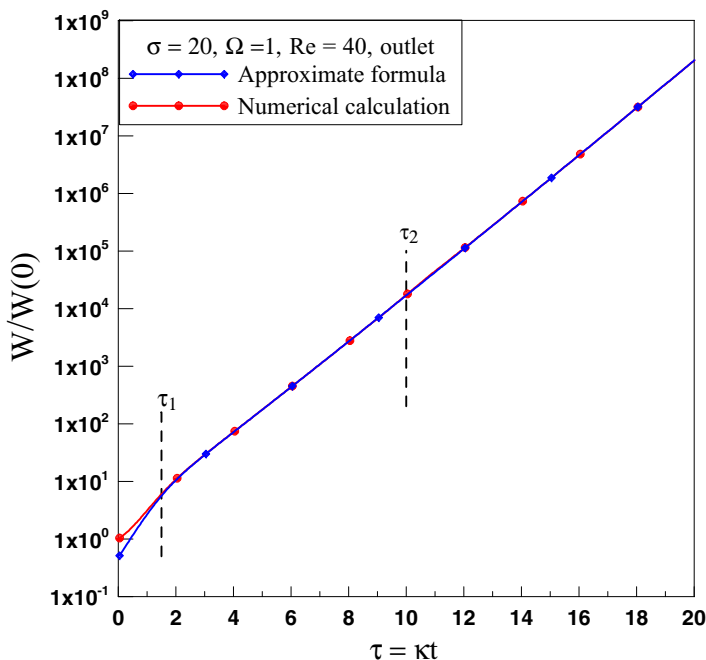


FIG. 14. Normalized total enstrophy for $\sigma = 20$, $\Omega = 1$, $\text{Re} = 40$, and initial disturbance orientation perpendicular to outlet direction (i.e., $\phi = \pi/2 - \psi = \pi/2 - \arctan \sqrt{\lambda} = 46.43^\circ$) calculated from the approximation (B4) (blue line) and numerically following the exact expression in the integral form (red line) given in Ref. [19]. The instants of time τ_1 and τ_2 correspond to changes in the asymptotic behavior from W_I to W_{II} and from W_{II} to W_{III} , respectively.

It should be noted that the above asymptotic expressions also approximate the exact expressions for the irrotational case ($\lambda = 1$). A comparison between a numerical calculation of the integral form and the above asymptotic expressions is presented in Fig. 14. Very good agreement is observed for $\tau > \tau_1$.

-
- [1] S. J. Kline, W. C. Reynolds, F. A. Schraub, and P. W. Runstadler, The structure of turbulent boundary layers, *J. Fluid Mech.* **30**, 741 (1967).
 - [2] H. T. Kim, S. J. Kline, and W. C. Reynolds, The production of turbulence near a smooth wall, *J. Fluid Mech.* **50**, 133 (1971).
 - [3] M. R. Head and P. Bandyopadhyay, New aspect of turbulent boundary-layers structure, *J. Fluid Mech.* **107**, 297 (1981).
 - [4] T. Theodorsen, Mechanism of turbulence, in *Proceedings of the Second Midwestern Conference on Fluid Mechanics* (Ohio State University, Columbus, 1952), p. 1.
 - [5] S. K. Robinson, Coherent motions in the turbulent boundary layers, *Annu. Rev. Fluid Mech.* **23**, 601 (1991).
 - [6] W. Schoppa and F. Hussain, Coherent structure generation in near wall turbulence, *J. Fluid Mech.* **453**, 57 (2002).
 - [7] K. M. Butler and B. F. Farrell, Three-dimensional optimal perturbations in viscous shear flow, *Phys. Fluids A* **4**, 1637 (1992).

- [8] S. C. Reddy, P. J. Schmid, J. S. Baggett, and D. S. Henningson, On the stability of streamwise streaks and transition thresholds in plane channel flows, *J. Fluid Mech.* **365**, 269 (1998).
- [9] T. Sayadi, C. W. Hamman, and P. Moin, Direct numerical simulation of complete H-type and K-type transitions with implications for the dynamics of turbulent boundary layers, *J. Fluid Mech.* **724**, 480 (2013).
- [10] F. Waleffe, On a self-sustaining process in shear flows, *Phys. Fluids* **9**, 883 (1997).
- [11] M. Farano, S. Cherubini, J.-C. Robinet, and P. De Palma, Hairpin-like optimal perturbations in plane Poiseuille flow, *J. Fluid Mech.* **775**, R2 (2015).
- [12] M. S. Acarlar and C. R. Smith, A study of hairpin vortices in a laminar boundary layer. Part 1. Hairpin vortices generated by a hemisphere protuberance, *J. Fluid Mech.* **175**, 1 (1987).
- [13] M. S. Acarlar and C. R. Smith, A study of hairpin vortices in a laminar boundary layer. Part 2. Hairpin vortices generated by fluid injection, *J. Fluid Mech.* **175**, 43 (1987).
- [14] E. Malkiel, V. Levinski, and J. Cohen, The evolution of a localized vortex disturbance in external shear flows. Part 2. Comparison with experiments in rotating shear flows, *J. Fluid Mech.* **379**, 351 (1999).
- [15] R. F. Blackwelder and J. H. Haritonidis, Scaling of the bursting frequency in turbulent boundary layers, *J. Fluid Mech.* **132**, 87 (1983).
- [16] J. D. Swearingen and R. F. Blackwelder, The growth and breakdown of streamwise vortices in the presence of a wall, *J. Fluid Mech.* **182**, 255 (1987).
- [17] V. Sponitsky, J. Cohen, and P. Z. Bar-Yoseph, The generation of streaks and hairpin vortices from a localized vortex embedded in unbounded uniform shear flow, *J. Fluid Mech.* **535**, 65 (2005).
- [18] J. Philip and J. Cohen, The evolution of a finite-amplitude localized disturbance in an irrotational unbounded plane stagnation flow, *J. Fluid Mech.* **555**, 459 (2006).
- [19] I. G. Shukhman, Evolution of a localized vortex in plane nonparallel viscous flows with constant velocity shear: I. Hyperbolic flow, *Phys. Fluids* **18**, 097101 (2006).
- [20] I. G. Shukhman, Evolution of a localized vortex in plane nonparallel viscous flows with constant velocity shear: II. Elliptic flow, *Phys. Fluids* **19**, 017106 (2007).
- [21] A. Leonard, *Turbulence Structure and Vortex Dynamics* (Cambridge University Press, Cambridge, 2000).
- [22] I. G. Shukhman and V. B. Levinski, The evolution of three-dimensionally localized vortices in shear flows. Linear theory, [arXiv:physics/0212101](https://arxiv.org/abs/physics/0212101) (2004).
- [23] I. G. Shukhman and V. Levinski, Temporal evolution of localized weak vortex in viscous circular shear flows, *Phys. Fluids* **17**, 017104 (2005).
- [24] J. Cohen, I. G. Shukhman, M. Karp, and J. Philip, An analytical-based method for studying the nonlinear evolution of localized vortices in planar homogenous shear flows, *J. Comput. Phys.* **229**, 7765 (2010).
- [25] J. Cohen, M. Karp, and V. Mehta, A minimal flow-elements model for the generation of packets of hairpin vortices in shear flows, *J. Fluid Mech.* **747**, 30 (2014).
- [26] R. R. Lagnado, N. Phan-Thien, and L. G. Leal, The stability of two-dimensional linear flows, *Phys. Fluids* **27**, 1094 (1984).
- [27] B. J. Bayly, Three-Dimensional Instability of Elliptical Flow, *Phys. Rev. Lett.* **57**, 2160 (1986).
- [28] M. J. Landman and P. G. Saffman, The three-dimensional instability of strained vortices in a viscous fluid, *Phys. Fluids* **30**, 2339 (1987).
- [29] J. C. R. Hunt, A. A. Wray, and P. Moin, Eddies, stream, and convergence zones in turbulent flows, in *Proceedings of Summer Program* (Centre for Turbulence Research, Stanford University, 1988), Report No. CTR-S88, p. 193.